High-resolution ultrastructure and morphology of marine ammonia-oxidizing archaea *Nitrosopumilus maritimus* SCM1 revealed by Cryo-ET and STEM-EDS

Yangkai Zhou[1]*, An Yan[2]*, Jiawen Yang[2,3]*, Wei He[1]*, Shuai Guo[2,3], Yifan Li[1], Yanchao Dai[4], Xijiang Pan[4], Dongyu Cui[1], Wenkai Teng[1], Olivier Pereira[1,5], Ran Bi[1], Songze Chen[1], Lu Fan[1], Peiyi Wang[2], Yan Liao[6], Wei Qin[7], Sen-Fang Sui[2,8], Yuanqing Zhu[1,9], Chuanlun Zhang[1,9]†, Zheng Liu[2]†

[1] Shenzhen Key Laboratory of Marine Archaea Geo-Omics, Department of Ocean Science and Engineering, Southern University of Science and Technology, Shenzhen, Guangdong, China

[2] Cryo-electron Microscopy Center, Southern University of Science and Technology, Shenzhen, Guangdong, China

[3] Department of Biology, Southern University of Science and Technology, Shenzhen, Guangdong Province, China

[4] Shanghai NanoPort, Thermo Fisher Scientific Inc., Shanghai, China

[5] Institut AMU-WUT, Aix-Marseille Université and Wuhan University of Technology, Wuhan, Hubei, China

[6] Australian Institute for Microbiology & Infection, University of Technology Sydney, Ultimo, Australia

[7] Department of Microbiology and Plant Biology and Institute for Environmental Genomics, University of Oklahoma, Norman, Oklahoma, USA

[8] State Key Laboratory of Membrane Biology, Beijing Frontier Research Center for Biological Structures, Beijing Advanced Innovation Center for Structural Biology, School of Life Sciences, Tsinghua University, Beijing, China

[9] Shanghai Sheshan National Geophysical Observatory, Shanghai, China

* These authors contributed equally.

† Correspondence: Chuanlun Zhang (zhangcl@sustech.edu.cn), Zheng Liu (liuz3@sustech.edu.cn).

Abstract

Nitrososphaerota, formerly known as Thaumarchaeota, constitutes a diverse and ubiquitous group of ammonia-oxidizing archaea (AOA) inhabiting ubiquitously in marine and terrestrial environments, playing a pivotal role in global nitrogen cycling. Despite their significance in Earth's ecosystems, the cellular organization of AOA remains largely unexplored, leading to a significant question unanswered of how the machinery of these organisms underpins metabolic functions. In this study, we combined chromatic-aberration-corrected cryo-electron tomography (Cryo-ET), scanning transmission electron microscopy (STEM), and energy dispersive X-ray spectroscopy (EDS) to unveil the cellular organization and elemental composition of *Nitrosopumilus maritimus* SCM1, a representative member of marine Nitrososphaerota. Our tomograms show the native ultrastructural morphology of SCM1 and find each cell contains one to several dense storage granules in the cytoplasm. STEM-EDS analysis identifies two types of storage granules with one type of granule being dominated by possibly polyphosphate and the other type being dominated by polyhydroxyalkanoate. The quantity of ribosomes in SCM1 are apparently an order of magnitude lower than that in eukaryotes and bacteria, supporting the slow growth of AOA commonly observed in the laboratory culture. Collectively, these findings provide visual evidence for the resilience of AOA in the vast oligotrophic marine environment.

Introduction

Comprehending the intricate cellular structure of microorganisms holds paramount importance in advancing our understanding of metabolic functions in ecology, evolution, and biogeochemistry (González-Pech et al., 2023). Despite remarkable advancements in cryo-electron microscopy (Cryo-EM) technology and the potential value of archaeal structural biology in medical and industrial applications (Shin et al., 2014), the realm of structural biology of marine archaea remains relatively underexplored, necessitating efforts to comprehensively grasp their cellular structure and physiological mechanisms (Lipp et al., 2008; Stahl and de la Torre, 2012).

Ammonia-oxidizing archaea (AOA) derives the energy from the oxidation of ammonia to nitrite, initiating nitrification process that is vital in the aquatic nitrogen cycle ((Stahl and de la Torre, 2012; Walker et al., 2010). The resulting nitrite, a byproduct of AOA activity, can be further transformed into nitrate by nitrite-oxidizing bacteria, and ultimately eliminated from the ecosystem as it converts into nitrogen gas through denitrifying bacteria (Martikainen, 2022). Notably, *Nitrosopumilus maritimus* SCM1 stands out as the first isolate of AOA (Konneke et al., 2005), exemplifying one of the most prevalent ammonia-oxidizing microbes in the oceans and actively driving global nitrogen cycling.

Previous studies have delved into various aspects of *Nitrosopumilus maritimus* SCM1, including its physiology like ammonium oxidation, stress adaptation, carbon fixation, genome, metabolome, lipidome, evolution and ecology (Abby et al., 2020; Hodgskiss et al., 2023; Kim et al., 2019; Kitzinger et al., 2020, 2019; Kraft et al., 2022; Law et al., 2021a, 2021b; Leavitt et al., 2023; Li et al., 2018; Martens-Habbena et al., 2009; Qin et al., 2020, 2018, 2014; Walker et al., 2010; Wan et al., 2023; Yang et al., 2021). However, our knowledge of its cellular structure remains limited. Within an archaeal cell, the cellular components are organized in a specific arrangement. Starting from the cell surface and moving inward, these components

83 typically include an s-layer, periplasmic space, cytoplasmic membrane, nucleoid,
84 ribosome. Additionally, certain archaeal cells may possess additional structures
85 like vesicles, archaellum and storage granules (van Wolferen et al., 2022). Several
86 studies have reported the presence of S-layer proteins on the surface of SCM1
87 cells, suggesting its existence as a cell wall (Qin et al., 2017; Urakawa et al., 2011).
88 Additionally, ribosomes have been observed in these cells. However, the cellular
89 structure of microorganisms, including for example, its presence and function of
90 storage granules, remains inadequately understood due to limited research efforts.
91 Storage granules play a pivotal role in microorganisms by enabling them to
92 withstand fluctuations in nutrient availability. Although extensive investigations
93 have been conducted on storage granules in certain bacterial, thermophilic
94 archaea, and eukaryotic organisms (Gal et al., 2017; Sarkar et al., 2021; Tocheva
95 et al., 2013; Toso et al., 2011, 2016; Ward et al., 2012), their existence and
96 functionality in marine archaea, particularly in SCM1, have yet to be explored. This
97 knowledge gap necessitates further exploration to unravel the cellular structure
98 and evaluate the presence and function of storage granules in marine archaea,
99 thereby expanding our understanding in this uncharted domain. Otherwise, no
100 high-resolution structures regarding the morphology of SCM1 cells in cell cycle
101 have been observed.
102

103 To bridge these knowledge gaps, we employed cutting-edge techniques, including
104 chromatic-aberration-corrected cryo-EM, cryo-electron tomography (cryo-ET),
105 scanning transmission electron microscopy (STEM) with energy-dispersive X-ray
106 spectroscopy (EDS), to comprehensively characterize the cellular structures of
107 SCM1. Our data present the high-resolution insights into the ultrastructure and
108 morphology of SCM1, shedding light on the potential metabolic functions of
109 storage granules in marine archaea. The use of chromatic-aberration-corrected
110 cryo-ET initiated in this study may represent an innovative technology for
111 effectively and comprehensively visualizing archaeal as well as bacterial cells at
112 submicron scales.

Results

Whole-cell cryo-electron tomography of *Nitrosopumilus maritimus* SCM1

We monitored cell growth in *Nitrosopumilus maritimus* SCM1 cultures by analyzing nitrite concentration. As shown in **Supplementary Figure 1**, during the nine days' cultivation period, nitrite concentration continued rise in the first seven days. We harvested SCM1 cells between day 6 and day 8, corresponding to the middle to later exponential phase. The purity of the cultures was evaluated using the qPCR method, and the results are presented in **Supplementary Table 1**.

Initially, we examined the morphology of *Nitrosopumilus maritimus* SCM1 cells by traditional cryo-EM. Our observations revealed that SCM1 cells showed a typical rod shape, with diameters ranging from 320 to 410 nm, lengths spanning from 590 to 1350 nm and the mean length-diameter ratio around 2.43 ± 0.57 (**Supplementary Figure 2**). Subsequently, cryo-ET experiment elucidated the cellular organization of SCM1 cells and provided a native three-dimensional (3D) structural information of the cell. Given the considerable thickness of the SCM1 (averaged diameter ~360nm, **Supplementary Figure 2**), the tilt-series image acquisition could not be completed. The thickness would double at ±60°, rendering it unsuitable for conventional cryo-EM data acquisition (**Supplementary Figure 3**). To overcome this difficulty, we employed the first chromatic-aberration-corrected cryo-EM in the world, of which can increase a signal/noise ratio for the thick specimens by corrected inelastic scattering. With the Cc corrector, images can be obtained at ±60°, and 3D tomogram can be reconstructed with less missing wedges. The 3D structure of native SCM1 revealed a highly organized proteinaceous surface layer (S-layer) enveloping the entire cell surface, and cell membrane exhibited well-defined, smooth, and continuous features (**Figure 1** and **Supplementary Movie 1**). Notably, an area rich in nucleic acids and dozens of ribosomes were observed in the cytoplasm of SCM1 (**Figure 1** and **Figure 2**) Interestingly, the number of ribosomes in SCM1 are ranged between ~30-100 in each cell, which appeared to be significant less than those found in eukaryotes

(Xing et al., 2023) or other prokaryotes (Xue et al., 2022) that observed by cryo-ET, lending a support for the slow growth of SCM1 that typically observed in the laboratory culture (**Supplementary Figure 1**).

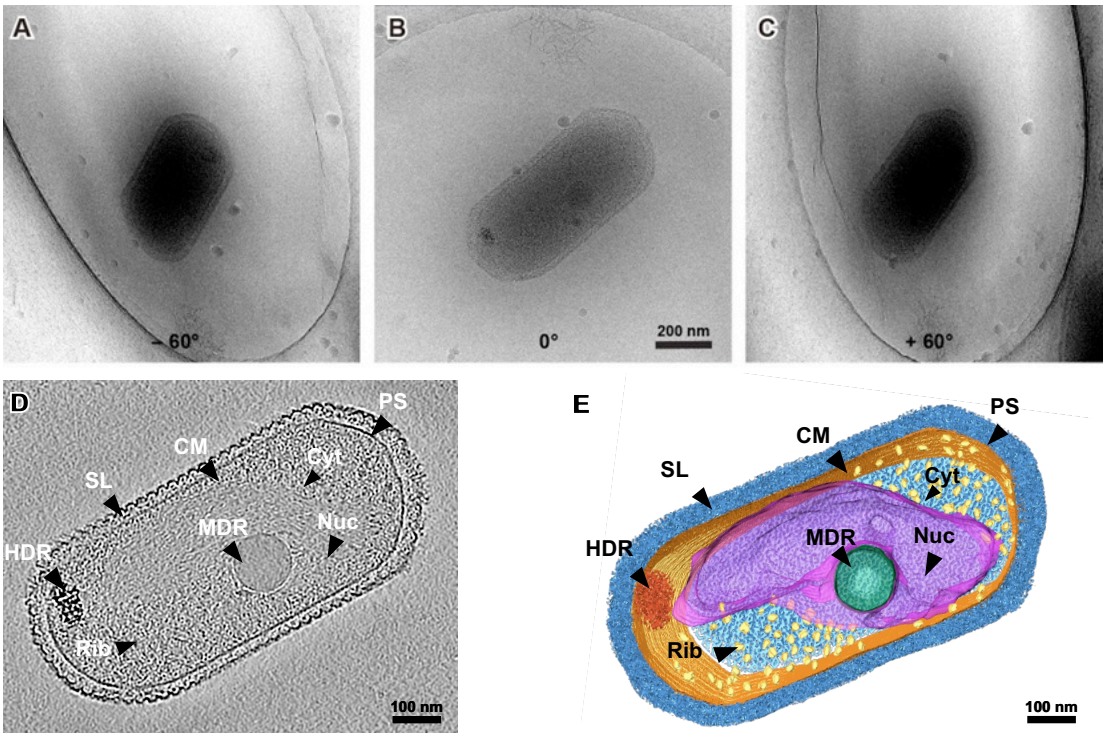

Figure 1. Whole-cell cryo-electron tomography of *Nitrosopumilus maritimus* SCM1.

(A-C) Cryo-EM images of SCM1 at – 60°, 0°, and + 60° angles. (D) Central section through a tomogram showed the cellular structure of SCM1. (E) 3D segmentation of SCM1 cell. MDR, medium-density region; HDR, high-density region; CM, cytoplasmic membrane; SL, surface layer; Nuc, nucleoid; Rib, ribosome; PS, periplasmic space; and Cyt, cytoplasm, are displayed.

151 **Observation of cell division in *Nitrosopumilus maritimus* SCM1**
152 To investigate the cell division process of SCM1, we examined several cells in the
153 exponential phase and identified instances of unequal divisions (**Figure 2A** and
154 **2B**). The central region of SCM1 first exhibited constriction, followed by elongation
155 towards two ends before eventually dividing into two cells (**Figure 2A**). Notably,
156 the cell division of SCM1 did not follow a homomorphic pattern, with the larger
157 daughter cell assuming an oblate spheroidal shape (**Figure 2A**), resembling the
158 shape of another independently observed cell in **Figure 2B**. Additionally, we
159 observed a putative budding state of SCM1 (**Figure 2C**).
160
161 Moreover, to determine the predominant mode of SCM1 cell division, we
162 conducted an intense measurement to observe changes in the diameter and length
163 of SCM1 in the late exponential phase. The results revealed two significant
164 decreases in the length of SCM1 within a 48-hour period, occurring at 11 PM on
165 the Day 6 and 7 AM on the Day 7, respectively (**Figure 2G**). However, no notable
166 change in diameter was observed within the 48-hour timeframe. The time interval
167 between the two decreasing points aligns with the doubling time of SCM1 (Td $\approx$
168 30 h, **Supplementary Figure 2**), which demonstrated high synchronicity of cell
169 division. Due to the dense sampling, we identified a cell in the pre-division state
170 (**Supplementary Figure 4**). In this state, putative scaffolds enclosed condensed
171 nucleoid and protein at one pole of the cell, leading to a noticeable increase in
172 electron density. Likewise, we have observed the presence of the similar
173 aggregates at the opposite pole of the cell, but no scaffolds found. Additionally, we
174 have noted that the S-layer protein on the cell surface forms an evenly distributed
175 hexatomic ring structure. Importantly, no division platform has been observed at
176 this particular stage.
177

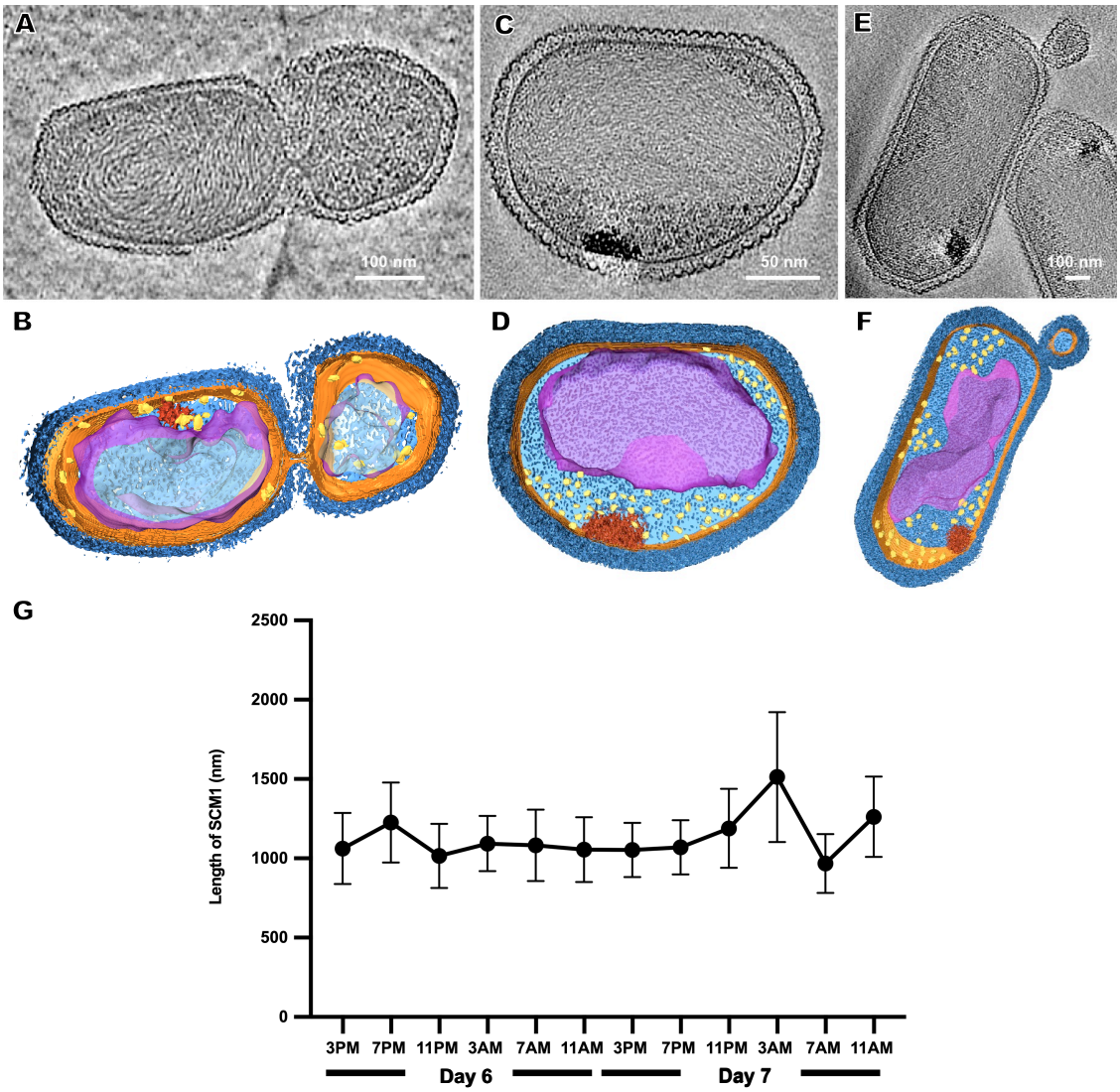

Figure 2. Observation of cell division in *Nitrosopumilus maritimus* SCM1. (A, C, E) Slices through tomograms of SCM1 in the exponential phase. (B, D, F) 3D segmentation of (A, C, E). S-layer (dark blue), cell membrane (orange); cytoplasm (light blue); nucleoid (purple); ribosomes (yellow); high-density region (red). (G) The average length of SCM1 at different time points. SCM1 cells were analyzed every 4 hours for 48 hours period in the late exponential phase (*n* = 40).

179 **Characterization of intracellular storage granules**

180 Our cryo-ET results revealed density regions corresponding to granule in the
181 cytoplasm of SCM1 (**Figure 1D** and **1E**). Based on differences in electronic density,
182 we classified them into medium-density regions (MDR) and high-density regions
183 (HDR). The MDR observed in SCM1 displayed a distinct and consistent spherical
184 morphology, with diameters typically ranging from approximately 85–185 nm, with
185 a smooth and continuous surface. The HDR exhibited an irregular shape and
186 comprised varying electronic density. Most HDRs were situated at the edge of cell,
187 near the cell membrane (**Figure 1** and **Figure 2**).

188

189 To analyze the elemental composition of MDR and HDR granules in the SCM1
190 cells, we used a Talos F200X to obtain EDS spectra. Area scans revealed
191 differential compositions of the granules, while HDRs containing elevated
192 concentrations of calcium, phosphorus, oxygen, and magnesium, the MDRs had a
193 slight increase in carbon concentration and a slightly lower concentration of oxygen
194 (**Figure 3** and **Supplementary Table 2**). Carbon and nitrogen were the most
195 abundant elements throughout the entire scanned region across the cells.

196

197 The mean Raman spectrum of SCM1 show main biomolecules in single cells
198 (**Figure 4A**). The Raman band at 1726 cm^{-1} can be assigned to
199 polyhydroxyalkanoate (PHA), which is contributed by the C=O ester stretching of
200 PHA (Spang et al., 2012). To further assess SCM1's potential to metabolize
201 storage granules and fully understand the metabolic potential at higher taxa, we
202 conducted an in-depth exploration of key metabolic pathways in *Nitrosopumilus*
203 *maritimus* SCM1, focusing on Polyphosphate (PolyP) and polyhydroxyalkanoate
204 (PHA) metabolism. The metabolic genes were involved in synthesis, degradation
205 or regulation. Through detailed genome annotation, we identified essential PHA-
206 related genes (K22881, K03821, K00019, K12405, K00074, and K00022) in SCM1.
207 However, we found no homologous genes associated with PolyP synthesis and
208 degradation in SCM1, despite the presence of intracellular PolyP confirmed by
209 STEM-EDS analysis. When considering a broader spectrum of AOA, we observed

210 the presence of PolyP-related genes (K00937, K22468, K23753, K01514, K01524)
211 and PHA-related genes (K22881, K03821, K00019, K12405, K00074, K00022)
212 across various strains. Notably, PolyP genes were identified in AOA strains ST2,
213 ST3, N4, Nd1, Nd2, CS, SbT1, SR1, EN76, G61, and MY3. Among these strains,
214 only ST2 and ST3 were found in marine habitats, specifically wastewater treatment
215 beside the ocean. The occurrence of Ppk2 genes in terrestrial AOA strains (CS,
216 SbT1, SR1, G61, MY3) highlighted the ecological diversity and metabolic versatility
217 within the AOA clade. Furthermore, the proteomic analysis of SCM1 emphasized
218 the importance of an S-layer biosynthesis gene, which was ranked as the most
219 abundant protein. This provided additional insights into the metabolic landscape of
220 SCM1. Meanwhile, the identification of PhaE and PhaC genes provided valuable
221 insights into PHA metabolism in SCM1. Overall, these findings contribute to our
222 understanding of the distribution of PolyP and PHA-related genes within AOA,
223 highlighting the unique metabolic profile of SCM1 compared to its counterparts.
224 (**Supplementary Table 3**).
225

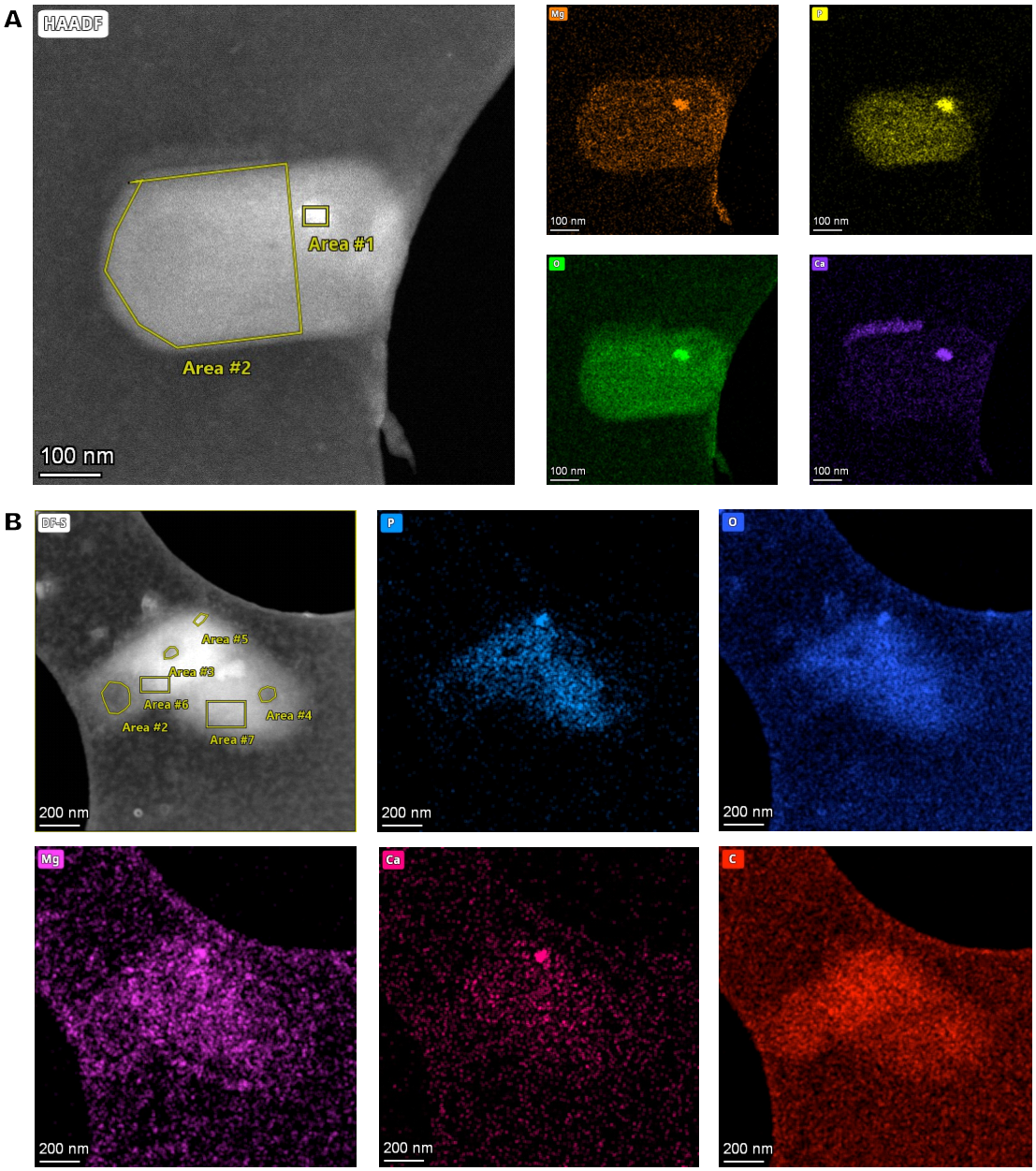

Figure 3. Elements in storage granules of SCM1.

(A) STEM images and EDS elemental analysis revealed that magnesium (Mg), phosphorus (P), oxygen (O), and calcium (Ca) in the Area #1 stood out from the background, indicating that enrichment of these elements in the HDR. (B) STEM-EDS results of two adjacent SCM1 cells. Area #5 is a HDR that enriched with Mg, P, O, and Ca. Area #2, 3, and 4 are MDRs with slightly higher concentration of carbon (C).

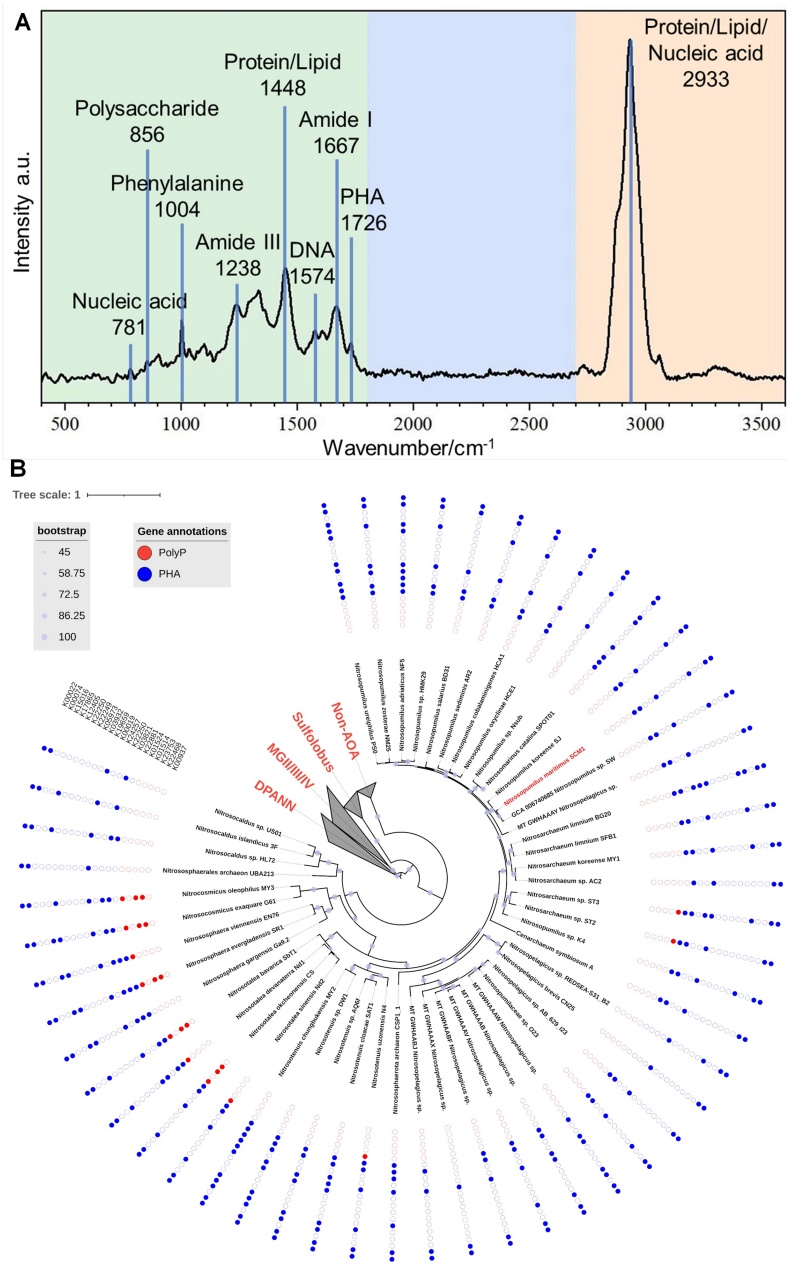

Figure 4. The Raman spectrum of *Nitrosopumilus maritimus* SCM1 and the distributions of metabolic genes regarding PolyP and PHA in AOA. (A) The mean Raman Spectrum of 33 single cells of SCM1. A characteristic peak of PHA at intensity = 1726 cm^{-1} was identified. (B) The phylogenomic tree of 51 nonredundant AOA genomes. The presence or absence of metabolic genes related to PolyP and PHA annotated by KEGG are shown around the tree. Solid dots: presence of the gene, empty dots: absence of the gene.

Discussion

According to previous studies, SCM1 owns two cell division systems in the gene, but only uses one system, the Cdv system, correlated with the eukaryotic ESCRT-III machinery, for cell division (Pelve et al., 2011; van Wolferen et al., 2022). However, the function of FtsZ system in SCM1 even in the whole Nitrososphaerota phylum, is not yet fully understood. Only one study has reported that the lack of polymerization function resulted in FtsZ not involving in the process of cell division (Ng et al., 2013). According to the cryo-EM images we captured, in addition to the fission state, we also observed SCM1 cells potentially in the budding state (**Figure 2E** and **2F**). A hypothesis is that the FtsZ system will be activated in the budding process. However, due to the limited number of SCM1 in the budding state we observed, we cannot exclude the possibility of being an extracellular membrane vesicle, just like those found in haloarchaea *Haloferax volcanii* (Ring and Eichler, 2001; Shalev et al., 2017; Tamir and Eichler, 2017).

Nutrition storage is crucial for microorganisms, providing resilience against fluctuations in nutrient availability. In the previous studies involving bacteria and archaea, similar storage granules had been analyzed using both electron energy loss spectroscopy (EELS) and energy dispersive X-ray spectroscopy (EDS) to determine their elemental composition (Lechaire et al., 2002; Remonsellez et al., 2006). In this study, STEM-EDS analysis has unveiled the intricate elemental composition of intracellular storage granules within *Nitrosopumilus maritimus* SCM1. The HDR granules exhibit heightened levels of phosphate, oxygen, and metals, suggesting their potential involvement in nutrient cycling and biogeochemical processes. The discovery of these storage granules opens intriguing avenues for unraveling SCM1's metabolic strategies and adaptive mechanisms.

In the early 20th century, ultrastructural investigations have already revealed the presence of polyphosphates granules in archaeal cells (Rudnick et al., 1990; Scherer and Bochem, 1983). Toso et al., introduced EDS analysis and

259 demonstrated the high abundance of phosphorus, oxygen and cationic elements
260 in polyphosphate bodies in *Methanospirillum hungatei* (Toso et al., 2011),
261 *Archaeoglobus fulgidus* (Toso et al., 2016) and ANME-2b (McGlynn et al., 2018).
262 Consistent to previous studies, the high concentration of phosphorus and oxygen,
263 along with cationic elements, suggests the presence of polyphosphate (PolyP) in
264 the HDR granules, which indicated that SCM1 may have a greater contribution to
265 global phosphorus cycling than previously recognized. Divalent cations, such as
266 magnesium and calcium, are known to form ionic bonds between phosphate
267 groups, enabling tighter packing and increased granule density (Parsons et al.,
268 2010).
269
270 The evidence pointing to the presence of PHA in SCM1, as indicated by STEM-
271 EDS, Raman spectroscopy, genome and proteome analyses, opens intriguing
272 avenues for understanding its physiological functions. While the exact function of
273 PHA in SCM1 remains to be elucidated, its potential role in carbon and energy
274 storage, similar to its function in haloarchaea, warrants further investigation. The
275 existence of PHA may contribute to SCM1's capacity to adapt to severe
276 environmental conditions or insufficient nutrient availability. The 3-
277 hydroxypropionate/4-hydroxybutyrate (3HP/4HB) cycle, discovered in ammonia-
278 oxidizing Nitrososphaerota, represents the most energy-efficient aerobic carbon
279 fixation pathway currently known (Johnson et al., 2023; Konneke et al., 2014).
280 According to the definition of the PHA synthesis/degradation pathway, Konneke
281 et al., found a key step involving the synthesis of PHA precursors in the carbon
282 cycle pathway of SCM1 (Konneke et al., 2014).
283
284 Our analysis of the PHA synthesis/degradation pathway, considering the presence
285 of key genes like *PhaEC* in the genome and proteome (**Figure 4B**), suggests that
286 under conditions of limited nutrition, such as depletion of bicarbonate ions, the
287 3HP/4HB cycle in SCM1 may not function normally. Instead, SCM1 could switch
288 to the biosynthesis pathway of PHA, utilizing carbon for survival. This adds
289 credence to the hypothesis of PHA's presence in SCM1 cells. Further exploration

290 of the role of PHA in SCM1's metabolism promises valuable insights into its
291 adaptive strategies. *PhaEC* and other genes we found on the genome and
292 proteome also helped us speculate that under conditions of limited nutrition (such
293 as depletion of bicarbonate ions), *3HP/4HB* cannot function normally and switches
294 to the biosynthesis pathway of PHA. Then SCM1 can use carbon to help itself
295 survive through the degradation pathway of PHA. This adds probability to the
296 presence of PHA in SCM1 cells.
297
298

299 **Materials and Methods**

300

301 ***Nitrosopumilus maritimus SCM1 cultivation***

302 We followed previous protocol for SCM1 cultivation, growth monitoring, and culture
303 purity assessment (Law et al., 2021b). To ensure the absence of bacterial and
304 organic contaminants during the long-term cultivation, we used a combination of
305 0.5 μg/ml Rifamycin sodium and 1 μg/ml hydrosoluble Amphotericin B. We
306 assessed cell growth by detecting nitrite production, which was determined by
307 diazo-colorimetric assay with photometric detection at 545 nm. For evaluating
308 culture purity, we employed quantitative real-time PCR (qPCR) to accurately
309 measure the culture's integrity and absence of contaminants, detailed data are
310 provided in **Supplementary Table 1**.

311

312 ***Collection and processing of Raman spectra of Nitrosopumilus maritimus***
313 ***SCM1***

314 *Nitrosopumilus maritimus* SCM1 was incubated at 30°C for 14 days. The pre-
315 treatment processes are as described previously (Wang et al., 2021). Single-cell
316 Raman spectra were acquired using a Raman imaging microscope (WITec alpha
317 300R) with 532 nm laser. All raw spectra were preprocessed with Project Five 5.2
318 (WITec) for baseline correction and vector normalization.

319

320 ***Cryo-EM sample preparation and data acquisition***

321 Quantifoil Cu R2/1 grids were glow discharged at 15 mA for 45 seconds using a
322 Pelco easiGlow discharged unit. An aliquot of 4 μL concentrated sample of SCM1
323 was applied to the front side of the grids, then the sample was vitrified by plunge
324 freezing in a liquid ethane using a Mark IV Vitrobot (Thermo Fisher Scientific) at
325 6 °C and 100% humidity. The vitrified samples were loaded into a 300-kV Titan
326 Krios microscopy G3i (Thermo Fisher Scientific) equipped with GIF quantum
327 energy filter and K2 Summit direct electron detector (Gatan Inc.). Images were

acquired using SerialEM package (Mastronarde, 2003) by the K2 camera operated under the super-resolution mode at a nominal magnification of ×26,000 (calibrated pixel size 5.417 Å). Each micrograph was fractionated into 36 frames with a total dose of 50 $e^{-}/Å^2$. The defocus range was set from −5.0 to −8.0 μm.

Cryo-ET data collection and tomogram reconstruction

For Cryo-ET, the vitrified samples were loaded into a 300-kV Titan Krios microscopy G4 (Thermo Fisher Scientific) equipped with Selectris energy filter and CEOS CCOR-spherical aberration / chromatic aberration (Cs/Cc) corrector. Tilt images were acquired by Falcon 4 camera under counting mode at a nominal magnification of ×26,000 (calibrated pixel size of 3.41 Å). A dose-symmetric scheme (Hagen et al., 2017) was used to collect tilt-series from -60° to +60° at a step size of 2° using SerialEM software (Mastronarde, 2003). Each tilt image was recorded as a video stack consisting of 10 frames with a dose of 1.64 $e^{-}/Å^2$. The defocus was set range from -4 to -6 μm and the total dose was 100 $e^{-}/Å^2$. Video frames of each tilt image were motion-corrected by MotionCor2 v.1.1.0 (Zheng et al., 2017). Tilt series were merged into one stack and aligned by patch tracking in IMOD v.4.9.12 (Kremer et al., 1996). In total, 221 sets of tilt-series were collected. The selected tomograms were reconstructed the missing-wedge information and increased signal-to-noise ratio by IsoNet (Liu et al., 2022) for display and segmentation by Amira (version 2020.3.1, Thermo Fisher Scientific).

STEM-EDS analysis

Samples are cryo-transferred by the Elsa™ holder (Gatan, model 698, ultra-low profile) and imaged in a Thermofisher Talos F200X transmission electron microscopy equipped with a Ceta camera in bright field mode, operated at a 200 kV acceleration voltage. Next, the cryo-holder with the sample was inserted into a pumping station to warm up to room temperature. Then a focused electron probe with high energy was used to stimulate a specific area of the sample. The atoms being stimulated may eject electrons, resulting in the emission of X-ray photons as a form of energy release. The energy exhibited by these X-rays is indicative of the

359 particular atomic element from which they originated. Therefore, an energy-
360 dispersive spectrometer can be employed to quantify the quantity and energy of
361 the X-rays, providing a quantitative description of the elemental composition of the
362 stimulated area of the sample (Toso et al., 2011). STEM-EDS tomography was
363 acquired at room temperature. The data process and 3D visualization were
364 performed by Inspect 3D and Avizo software.
365
366 ***Gene and genomic analysis***
367 Phylogenomic analysis of Nitrososphaerota was conducted using IQ-TREE with
368 GTDB archaeal markers obtained from the Genome Taxonomy Database. The
369 selected markers were carefully aligned using MAFFT and then concatenated into
370 a supermatrix. The best-fitting substitution model was determined using
371 ModelFinder, and the phylogenomic tree was constructed using Maximum
372 Likelihood with ultrafast bootstrap approximation. The genomes were curated as
373 our previous study. The PolyP and PHA related protein sequences were aligned
374 to KEGG database using HMM search. The KO numbers of PolyP related genes
375 are: K00937(*Ppk1*), K22468(*Ppk2*), K23753(*Ppk2*), K01514(*PPX1*),
376 K01524(*Ppx/GppA*), and PHA related genes are: K22881(*PhaE*), K03821(*PhaC*),
377 K22250(*PhaB*), K24257(*PhaR*), K00019(*PhaZh1/BdhA*), K19659(*PhaJ*),
378 K03932(*PhaZ1*), K05973(*PhaZ*), K22249(*PhaZ*), K22250(*PhaZ*),
379 K12405(hydratase), K17865(hydratase), K15016(hydratase),
380 K00074(dehrogenase), K00022(dehrogenase). Functional domains of PHA
381 regulation genes PhaJ and BdhA were checked in InterProScan. The resulting tree
382 was beautified using the Interactive Tree of Life (iTOL) web tool. The Newick-
383 formatted tree was uploaded to iTOL, where branches were colorized, additional
384 annotations were added, and the overall appearance of the tree was customized
385 for better clarity and aesthetics.
386
387 ***Proteome analysis***

388 Filters containing late exponential phase *Nitrosopumilus maritimus* SCM1 cells
389 were extracted using a modified protocol as described before (Qin et al., 2018),
390 either trypsin or GluC was used as protease digestion. Mass spectrometry analysis
391 was carried out at Shenzhen Wininnovate BioTechnology Co., Ltd. DDA (data-
392 dependent acquisition) mass spectrum techniques were used to acquire tandem
393 MS data on a ThermoFisher Q Exactive mass spectrometer fitted with a Nano Flex
394 ion source. The raw MS/MS spectra were treated and searched against the NCBI
395 and UniProt Proteome dataset using MaxQuant 2.0.3.0. The generated data set
396 contains the results of different hydrolases and databases for comparison.

397

398 **Acknowledgements**

399 We thank Huiqin Xu, Xiaoyun Yang, and Zongqiang Li for assistance on
400 experiment design. Jing Wu, Yuanzhu Gao, Juying Tan, and Fangfang Zhang for
401 technical support. This study was supported by the Stable Support Plan Program
402 of Shenzhen Natural Science Fund (20200925173954005), National Natural
403 Science Foundation of China (32241028 and 91851210), the Shenzhen Key
404 Laboratory of Marine Archaea Geo-Omics, Southern University of Science and
405 Technology (ZDSYS201802081843490), and the Project of Educational
406 Commission of Guangdong Province of China (2020KTSCX123). The
407 bioinformatic analyses were performed on the Tai-Yi high-performance
408 supercomputer cluster at Southern University of Science and Technology.

409

410 **Author contributions**

411 ZL, CZ designed the study. YZ, AY, JY, WH performed the sample preparation,
412 data analyses, and wrote the manuscript. SG conducted the reconstruction of
413 Cryo-ET data. YL prepared cell cultures, performed the sample preparation
414 experiment. YD, XP performed the STEM-EDS analyses. DC performed the
415 Raman spectrum analyses. WT, OP, RB, SC, LF assisted the lab work or data
416 analyses. PW, SS provided platforms. WQ, YL assisted study design, data

interpretation and manuscript editing. ZL, CZ supervised the investigation and revised manuscript.

Competing interests

The authors declare no conflict of interest.

References

Abby SS, Kerou M, Schleper C. 2020. Ancestral Reconstructions Decipher Major Adaptations of Ammonia-Oxidizing Archaea upon Radiation into Moderate Terrestrial and Marine Environments. *mBio* **11**:e02371-20. doi:10.1128/mBio.02371-20

Gal A, Sviben S, Wirth R, Schreiber A, Lassalle‐Kaiser B, Faivre D, Scheffel A. 2017. Trace‐Element Incorporation into Intracellular Pools Uncovers Calcium‐Pathways in a Coccolithophore. *Advanced Science* **4**:1700088. doi:10.1002/advs.201700088

González-Pech RA, Li VY, Garcia V, Boville E, Mammone M, Kitano H, Ritchie KB, Medina M. 2023. The Evolution, Assembly, and Dynamics of Marine Holobionts. *Annual Review of Marine Science* **16**:11.1-11.24. doi:10.1146/annurev-marine-022123-104345

Hagen WJH, Wan W, Briggs JAG. 2017. Implementation of a cryo-electron tomography tilt-scheme optimized for high resolution subtomogram averaging. *Journal of Structural Biology* **197**:191–198. doi:10.1016/j.jsb.2016.06.007

Hodgskiss LH, Melcher M, Kerou M, Chen W, Ponce-Toledo RI, Savvides SN, Wienkoop S, Hartl M, Schleper C. 2023. Unexpected complexity of the ammonia monooxygenase in archaea. *The ISME Journal* **17**:588-599. doi:10.1038/s41396-023-01367-3

Johnson J, Tolar BB, Tosun B, Yoshikuni Y, Francis CA, Wakatsuki S, DeMirci H. 2023. Crystal Structure of 4-Hydroxybutyryl-CoA Synthetase (ADP-forming): A Key Enzyme in the Thaumarchaeal Hydroxypropionate/Hydroxybutyrate cycle. *bioRxiv*. doi:10.1101/2023.07.14.549078

Kim J-G, Kim S-J, Cvirkaite-Krupovic V, Yu W-J, Gwak J-H, López-Pérez M, Rodriguez-Valera F, Krupovic M, Cho J-C, Rhee S-K. 2019. Spindle-shaped viruses infect marine ammonia-oxidizing thaumarchaea. *Proc Natl Acad Sci USA* **116**:15645–15650. doi:10.1073/pnas.1905682116

Kitzinger K, Marchant HK, Bristow LA, Herbold CW, Padilla CC, Kidane AT, Littmann S, Daims H, Pjevac P, Stewart FJ, Wagner M, Kuypers MMM. 2020. Single cell analyses reveal contrasting life strategies of the two main nitrifiers in the ocean. *Nat Commun* **11**:767. doi:10.1038/s41467-020-14542-3

Kitzinger K, Padilla CC, Marchant HK, Hach PF, Herbold CW, Kidane AT, Konneke M, Littmann S, Mooshammer M, Niggemann J, Petrov S, Richter A, Stewart FJ, Wagner M, Kuypers MMM, Bristow LA. 2019. Cyanate and urea are substrates for nitrification by Thaumarchaeota in the marine environment. *Nat Microbiol* **4**:234–243. doi:10.1038/s41564-018-0316-2

Konneke M, Bernhard AE, de la Torre JR, Walker CB, Waterbury JB, Stahl DA. 2005. Isolation of an autotrophic ammonia-oxidizing marine archaeon. *Nature* **437**:543–6. doi:10.1038/nature03911

Konneke M, Schubert DM, Brown PC, Hugler M, Standfest S, Schwander T, Schada von Borzyskowski L, Erb TJ, Stahl DA, Berg IA. 2014. Ammonia-oxidizing archaea use the most energy-efficient aerobic pathway for CO2 fixation. *Proc Natl Acad Sci U S A* **111**:8239–44. doi:10.1073/pnas.1402028111

Kraft B, Jehmlich N, Larsen M, Bristow LA, Könneke M, Thamdrup B, Canfield DE. 2022. Oxygen and nitrogen production by an ammonia-oxidizing archaeon. *Science* **375**:97–100. doi:10.1126/science.abe6733

Kremer JR, Mastronarde DN, McIntosh JR. 1996. Computer Visualization of Three-Dimensional Image Data Using IMOD. *Journal of Structural Biology* **116**:71–76. doi:10.1006/jsbi.1996.0013

Law KP, He W, Tao J, Zhang C. 2021a. A Novel Approach to Characterize the Lipidome of Marine Archaeon *Nitrosopumilus maritimus* by Ion Mobility Mass Spectrometry. *Frontiers in Microbiology* **12**.

Law KP, He W, Tao J, Zhang C. 2021b. Characterization of the Exometabolome of *Nitrosopumilus maritimus* SCM1 by Liquid Chromatography–Ion Mobility Mass Spectrometry. *Frontiers in Microbiology* **12**.

Leavitt WD, Kopf SH, Weber Y, Chiu B, McFarlin JM, Elling FJ, Hoeft-McCann S, Pearson A. 2023. Controls on the hydrogen isotope composition of tetraether lipids in an autotrophic ammonia-oxidizing marine archaeon. *Geochimica et Cosmochimica Acta* **352**:194-210. doi:10.1016/j.gca.2023.04.033

Lechaire J, Shillito B, Frébourg G, Gaill F. 2002. Elemental characterization of microorganism granules by EFTEM in the tube wall of a deep‐sea vent invertebrate. *Biology of the Cell* **94**:243–249. doi:10.1016/s0248-4900(02)01199-1

Li P-N, Herrmann J, Tolar BB, Poitevin F, Ramdasi R, Bargar JR, Stahl DA, Jensen GJ, Francis CA, Wakatsuki S, van den Bedem H. 2018. Nutrient transport suggests an evolutionary basis for charged archaeal surface layer proteins. *The ISME Journal* **12**:2389–2402. doi:10.1038/s41396-018-0191-0

Lipp JS, Morono Y, Inagaki F, Hinrichs K-U. 2008. Significant contribution of Archaea to extant biomass in marine subsurface sediments. *Nature* **454**:991–994. doi:10.1038/nature07174

Liu Y-T, Zhang H, Wang H, Tao C-L, Bi G-Q, Zhou ZH. 2022. Isotropic reconstruction for electron tomography with deep learning. *Nat Commun* **13**:6482. doi:10.1038/s41467-022-33957-8

Martens-Habbena W, Berube PM, Urakawa H, de la Torre JR, Stahl DA. 2009. Ammonia oxidation kinetics determine niche separation of nitrifying Archaea and Bacteria. *Nature* **461**:976–979. doi:10.1038/nature08465

Martikainen PJ. 2022. Heterotrophic nitrification – An eternal mystery in the nitrogen cycle. *Soil Biology and Biochemistry* **168**:108611. doi:10.1016/j.soilbio.2022.108611

Mastronarde DN. 2003. SerialEM: A Program for Automated Tilt Series Acquisition on Tecnai Microscopes Using Prediction of Specimen Position. *Microsc Microanal* **9**:1182–1183. doi:10.1017/s1431927603445911

McGlynn SE, Chadwick GL, O'Neill A, Mackey M, Thor A, Deerinck TJ, Ellisman MH, Orphan VJ. 2018. Subgroup Characteristics of Marine Methane-Oxidizing ANME-2 Archaea and Their Syntrophic Partners as Revealed by Integrated Multimodal Analytical Microscopy. *Appl Environ Microbiol* **84**:e00399-18. doi:10.1128/AEM.00399-18

Ng K-H, Srinivas V, Srinivasan R, Balasubramanian M. 2013. The *Nitrosopumilus maritimus* CdvB, but Not FtsZ, Assembles into Polymers. *Archaea* **2013**:1–10. doi:10.1155/2013/104147

Parsons AJ, Ahmed I, Rudd CD, Cuello GJ, Pellegrini E, Richard D, Johnson MR. 2010. Neutron scattering and*ab initio*molecular dynamics study of cross-linking in biomedical phosphate glasses. *J Phys: Condens Matter* **22**:485403. doi:10.1088/0953-8984/22/48/485403

Pelve EA, Lindås A-C, Martens-Habbena W, de la Torre JR, Stahl DA, Bernander R. 2011. Cdv-based cell division and cell cycle organization in the thaumarchaeon *Nitrosopumilus maritimus*. *Molecular Microbiology* **82**:555–566. doi:10.1111/j.1365-2958.2011.07834.x

Qin W, Amin SA, Lundeen RA, Heal KR, Martens-Habbena W, Turkarslan S, Urakawa H, Costa KC, Hendrickson EL, Wang T, Beck DA, Tiquia-Arashiro SM, Taub F, Holmes AD, Vajrala N, Berube PM, Lowe TM, Moffett JW, Devol AH, Baliga NS, Arp DJ, Sayavedra-Soto LA, Hackett M, Armbrust EV, Ingalls AE, Stahl DA. 2018. Stress response of a marine ammonia-oxidizing archaeon informs physiological status of environmental populations. *The ISME Journal* **12**:508–519. doi:10.1038/ismej.2017.186

Qin W, Amin SA, Martens-Habbena W, Walker CB, Urakawa H, Devol AH, Ingalls AE, Moffett JW, Armbrust EV, Stahl DA. 2014. Marine ammonia-oxidizing archaeal isolates display obligate mixotrophy and wide ecotypic variation. *Proc Natl Acad Sci U S A* **111**:12504–9. doi:10.1073/pnas.1324115111

Qin W, Heal KR, Ramdasi R, Kobelt JN, Martens-Habbena W, Bertagnolli AD, Amin SA, Walker CB, Urakawa H, Konneke M, Devol AH, Moffett JW, Armbrust EV, Jensen GJ, Ingalls AE, Stahl DA. 2017. *Nitrosopumilus maritimus* gen. nov., sp. nov., *Nitrosopumilus cobalaminigenes* sp. nov., *Nitrosopumilus oxyclinae* sp.

538 nov., and *Nitrosopumilus ureiphilus* sp. nov., four marine ammonia-oxidizing
539 archaea of the phylum Thaumarchaeota. *Int J Syst Evol Microbiol* **67**:5067–5079.
540 doi:10.1099/ijsem.0.002416

541 Qin W, Zheng Y, Zhao F, Wang Y, Urakawa H, Martens-Habbena W, Liu H,
542 Huang X, Zhang X, Nakagawa T, Mende DR, Bollmann A, Wang B, Zhang Y,
543 Amin SA, Nielsen JL, Mori K, Takahashi R, Virginia Armbrust E, Winkler M-KH,
544 DeLong EF, Li M, Lee P-H, Zhou J, Zhang C, Zhang T, Stahl DA, Ingalls AE.
545 2020. Alternative strategies of nutrient acquisition and energy conservation map
546 to the biogeography of marine ammonia-oxidizing archaea. *The ISME Journal*
547 **14**:2595–2609. doi:10.1038/s41396-020-0710-7

548 Remonsellez F, Orell A, Jerez CA. 2006. Copper tolerance of the
549 thermoacidophilic archaeon Sulfolobus metallicus: possible role of polyphosphate
550 metabolism. *Microbiology* **152**:59–66. doi:10.1099/mic.0.28241-0

551 Ring G, Eichler J. 2001. Characterization of Inverted Membrane Vesicles from
552 the Halophilic Archaeon Haloferax volcanii. *Journal of Membrane Biology*
553 **183**:195–204. doi:10.1007/s00232-001-0067-4

554 Rudnick H, Hendrich S, Pilatus U, Blotevogel K-H. 1990. Phosphate
555 accumulation and the occurrence of polyphosphates and cyclic 2,3-
556 diphosphoglycerate in Methanosarcina frisia. *Arch Microbiol* **154**.
557 doi:10.1007/BF00248840

558 Sarkar P, Shukla MR, Kumbhar P, Manjre S, Dasgupta S, Bhakthavatsalam V.
559 2021. Intracellular Localization of Micronutrients in Algae Cells Using Scanning
560 Transmission Electron Microscopy–Energy-Dispersive X-ray Spectroscopy
561 (STEM-EDX) In: Ghosal P, Carter CB, Vinothkumar KR, Sarkar R, editors.
562 Applications of Microscopy in Materials and Life Sciences, Springer Proceedings
563 in Materials. Singapore: Springer. pp. 203–210. doi:10.1007/978-981-16-2982-
564 2_20

565 Scherer PA, Bochem H-P. 1983. Ultrastructural investigation of 12
566 Methanosarcinae and related species grown on methanol for occurrence of
567 polyphosphatelike inclusions. *Can J Microbiol* **29**:1190–1199. doi:10.1139/m83-
568 182

569 Shalev Y, Turgeman-Grott I, Tamir A, Eichler J, Gophna U. 2017. Cell Surface
570 Glycosylation Is Required for Efficient Mating of Haloferax volcanii. *Frontiers in*
571 *Microbiology* **8**. doi:10.3389/fmicb.2017.01253

572 Shin DS, Pratt AJ, Tainer JA. 2014. Archaeal Genome Guardians Give Insights
573 into Eukaryotic DNA Replication and Damage Response Proteins. *Archaea*
574 **2014**:1–24. doi:10.1155/2014/206735

575 Spang A, Poehlein A, Offre P, Zumbrägel S, Haider S, Rychlik N, Nowka B,
576 Schmeisser C, Lebedeva EV, Rattei T, Böhm C, Schmid M, Galushko A,
577 Hatzenpichler R, Weinmaier T, Daniel R, Schleper C, Spieck E, Streit W, Wagner

578 M. 2012. The genome of the ammonia-oxidizing Candidatus *Nitrososphaera*
579 *gargensis*: insights into metabolic versatility and environmental adaptations.
580 *Environmental Microbiology* **14**:3122–3145. doi:10.1111/j.1462-
581 2920.2012.02893.x

582 Stahl DA, de la Torre JR. 2012. Physiology and Diversity of Ammonia-Oxidizing
583 Archaea. *Annu Rev Microbiol* **66**:83–101. doi:10.1146/annurev-micro-092611-
584 150128

585 Tamir A, Eichler J. 2017. N-Glycosylation Is Important for Proper Haloferax
586 volcanii S-Layer Stability and Function. *Appl Environ Microbiol* **83**:e03152-16.
587 doi:10.1128/AEM.03152-16

588 Tocheva EI, Dekas AE, McGlynn SE, Morris D, Orphan VJ, Jensen GJ. 2013.
589 Polyphosphate Storage during Sporulation in the Gram-Negative Bacterium
590 Acetonema longum. *Journal of Bacteriology* **195**:3940–3946.
591 doi:10.1128/JB.00712-13

592 Toso DB, Henstra AM, Gunsalus RP, Zhou ZH. 2011. Structural, mass and
593 elemental analyses of storage granules in methanogenic archaeal cells.
594 *Environmental Microbiology* **13**:2587–2599. doi:10.1111/j.1462-
595 2920.2011.02531.x

596 Toso DB, Javed MM, Czornyj E, Gunsalus RP, Zhou ZH. 2016. Discovery and
597 Characterization of Iron Sulfide and Polyphosphate Bodies Coexisting
598 in*Archaeoglobus fulgidus*Cells. *Archaea* **2016**:1–11. doi:10.1155/2016/4706532

599 Urakawa H, Martens-Habbena W, Stahl DA. 2011. Physiology and Genomics of
600 Ammonia-Oxidizing ArchaeaNitrification. John Wiley & Sons, Ltd. pp. 115–155.

601 van Wolferen M, Pulschen AA, Baum B, Gribaldo S, Albers S-V. 2022. The cell
602 biology of archaea. *Nat Microbiol* **7**:1744-1755. doi:10.1038/s41564-022-01215-8

603 Walker CB, de la Torre JR, Klotz MG, Urakawa H, Pinel N, Arp DJ, Brochier-
604 Armanet C, Chain PS, Chan PP, Gollabgir A, Hemp J, Hugler M, Karr EA,
605 Konneke M, Shin M, Lawton TJ, Lowe T, Martens-Habbena W, Sayavedra-Soto
606 LA, Lang D, Sievert SM, Rosenzweig AC, Manning G, Stahl DA. 2010.
607 *Nitrosopumilus maritimus* genome reveals unique mechanisms for nitrification
608 and autotrophy in globally distributed marine crenarchaea. *Proc Natl Acad Sci U*
609 *S A* **107**:8818–23. doi:10.1073/pnas.0913533107

610 Wan XS, Hou L, Kao S-J, Zhang Y, Sheng H-X, Shen H, Tong S, Qin W, Ward
611 BB. 2023. Pathways of N_2O production by marine ammonia-oxidizing archaea
612 determined from dual-isotope labeling. *Proc Natl Acad Sci USA*
613 **120**:e2220697120. doi:10.1073/pnas.2220697120

614 Wang Y, Xu J, Cui D, Kong L, Chen S, Xie W, Zhang C. 2021. Classification and
615 Identification of Archaea Using Single-Cell Raman Ejection and Artificial

616 Intelligence: Implications for Investigating Uncultivated Microorganisms. *Anal*
617 *Chem* **93**:17012–17019. doi:10.1021/acs.analchem.1c03495

618 Ward SK, Heintz JA, Albrecht RM, Talaat AM. 2012. Single-Cell Elemental
619 Analysis of Bacteria: Quantitative Analysis of Polyphosphates in Mycobacterium
620 tuberculosis. *Frontiers in Cell and Infection Microbiology* **2**.
621 doi:10.3389/fcimb.2012.00063

622 Xing H, Taniguchi R, Khusainov I, Kreysing JP, Welsch S, Turoňová B, Beck M.
623 2023. Translation dynamics in human cells visualized at high resolution reveal
624 cancer drug action. *Science* **381**:70–75. doi:10.1126/science.adh1411

625 Xue L, Lenz S, Zimmermann-Kogadeeva M, Tegunov D, Cramer P, Bork P,
626 Rappsilber J, Mahamid J. 2022. Visualizing translation dynamics at atomic detail
627 inside a bacterial cell. *Nature* **610**:205–211. doi:10.1038/s41586-022-05255-2

628 Yang Y, Zhang C, Lenton TM, Yan X, Zhu M, Zhou M, Tao J, Phelps TJ, Cao Z.
629 2021. The Evolution Pathway of Ammonia-Oxidizing Archaea Shaped by Major
630 Geological Events. *Molecular Biology and Evolution* **38**:3637–3648.
631 doi:10.1093/molbev/msab129

632 Zheng SQ, Palovcak E, Armache J-P, Verba KA, Cheng Y, Agard DA. 2017.
633 MotionCor2: anisotropic correction of beam-induced motion for improved cryo-
634 electron microscopy. *Nat Methods* **14**:331–332. doi:10.1038/nmeth.4193

635